




**Constrained large-eddy simulation of turbulent flow over rough walls**Wen Zhang,<sup>1</sup> Minping Wan ,<sup>1,2,3,\*</sup> Zhenhua Xia ,<sup>4</sup> Jianchun Wang ,<sup>1,2,3</sup>  
Xiyun Lu,<sup>5</sup> and Shiyi Chen<sup>1,2,3,†</sup><sup>1</sup>*Guangdong Provincial Key Laboratory of Turbulence Research and Applications, Southern University of Science and Technology, Shenzhen, Guangdong 518055, People's Republic of China*<sup>2</sup>*Guangdong-Hong Kong-Macao Joint Laboratory for Data-Driven Fluid Mechanics and Engineering Applications, Southern University of Science and Technology, Shenzhen 518055, China*<sup>3</sup>*Southern Marine Science and Engineering Guangdong Laboratory (Guangzhou), 1119 Haibin Road, Nansha District, Guangzhou 511458, China*<sup>4</sup>*Department of Engineering Mechanics, Zhejiang University, Hangzhou, Zhejiang 310027, People's Republic of China*<sup>5</sup>*Department of Modern Mechanics, University of Science and Technology of China, Hefei, Anhui 230026, People's Republic of China*

(Received 24 October 2020; accepted 18 March 2021; published 5 April 2021)

Recent research indicates that the structure of the wall-bounded turbulence depends on the mean shear created by the wall. To examine the response of the wall turbulence to the rough-wall-like mean shear, we performed numerical tests of the channel flows in the framework of the constrained large-eddy simulation without resolving the roughness elements. Once the rough-wall-like mean shear is imposed, the normalized contribution of the sweep motions to the Reynolds stress increases in the near-wall region and the two-point correlation of the streamwise velocity in the outer layer is enhanced. The constraint of the rough-wall-like mean shear provides extra resistance just like the surface roughness, which is observed via the decomposition of the skin friction coefficient. All the statistics indicate that the effect of the rough-wall-like mean shear on the turbulent flow is similar to the effect of roughness elements. The large-eddy simulations of the rough-wall flows using the conventional equilibrium-wall model are also performed for comparison. The statistical results in the outer layer are qualitatively consistent with those obtained by constraining the mean shear, which demonstrates the latter approach can be used as a new wall model for the simulation of the rough-wall flows.

DOI: [10.1103/PhysRevFluids.6.044602](https://doi.org/10.1103/PhysRevFluids.6.044602)**I. INTRODUCTION**

The turbulent flow over the rough walls occurs in a wide range of industrial and geophysical flows. The wall friction of pipes or ship hulls is greatly increased by the roughness so that more energy is needed to overcome the resistance [1–4]. The efficiencies of the energy transfer and the carbon dioxide exchange in the atmospheric boundary layer are greatly affected by the surface roughness formed by the plants and buildings [5–8]. In terms of how the near-wall turbulence is modified by the surface roughness, it is still not fully understood despite the many efforts in the past decades.

As reviewed by Jimenez [9], recent research indicates that it is the mean shear that determines the turbulence structure, and the wall is just required to create the mean shear. Tuerke and Jimenez [10] performed direct numerical simulations of turbulent channels with an artificially prescribed mean velocity profile. They found that the natural turbulent flow can be reproduced correctly when

\*wanmp@sustech.edu.cn

†chensy@sustech.edu.cn

the natural distribution of the mean velocity is prescribed, but a significant change occurs once the mean shear is modified. This indicates that the mean shear has a great impact on the wall turbulence. Lozano-Duran and Bae [11] simulated the channel flows driven by the nonuniform body forces and found that the flow structures are substantially altered to accommodate the new mean momentum transfer. Thus they proposed a hypothesis that the momentum-carrying eddies are controlled by the local mean shear rather than the distance to the wall. Similarly, Davidson and Krogstad [12] proposed a universal scaling theory for both the smooth- and rough-wall flows, in which the local mean shear is used instead of the wall distance. Recently, Bae *et al.* [13] applied the slip-wall condition to solve the problem of the wall-stress underestimation in large-eddy simulation. These results indicate that the detailed wall condition may not be that important if the mean shear can be correctly provided in the simulation of wall turbulence.

On the rough walls, the mean shear is modified by the surface roughness, as demonstrated by the downward shift of the mean streamwise velocity profile. Then how will the wall turbulence behave when a rough-wall-like mean shear is prescribed without resolving the roughness elements? Will the effect of the rough-wall-like mean shear be similar to that of the surface roughness? To answer these questions, we carried out numerical tests in the framework of constrained large-eddy simulation (CLES) [14]. In this approach, the rough-wall-like mean shear is imposed via constraining the subgrid-scale stress in the near-wall region.

This paper is organized as follows. In Sec. II, the previous research about the turbulent flow over rough walls and the approach of the CLES are briefly reviewed. In Sec. III, the numerical methods are introduced. In Sec. IV, the test cases and the simulation results are presented and discussed. Finally, in Sec. VI the conclusions of this work are summarized.

## II. BACKGROUND

### A. Turbulent flow over rough walls

Most of the turbulent kinetic energy in the wall-bounded turbulence is generated via the nonlinear self-sustaining cycle in the buffer region between  $10 < y^+ < 100$ , where  $y$  is the wall distance and the superscript “+” represents the quantity normalized in wall units. This cycle is characterized by the violent ejection of the low speed fluid towards the outer layer, and immediately followed by the sweep of the high speed fluid into the near wall region. As the height of the roughness elements increases, the nonlinear self-sustaining cycle [15] in the buffer region of wall turbulence can be modified or even completely destroyed on the rough walls [16].

Using the conditional statistics of the Reynolds stress, Raupach [17] found that the sweep (Q4) accounts for most of the stress near the roughness layer. The increased contribution to the Reynolds stress from the sweep in the near-wall region is also observed in other experiments or simulations with various types of surface roughness, such as mesh-screen roughness [18–22]. The sweep motion is generated by the downdraft between a pair of counter-rotating streamwise vortices [6]. Krogstad and Antonia [23] found that the inclination angle of the streamwise vortex structures increases from  $10^\circ$  on the smooth wall to  $38^\circ$  on the mesh-screen rough wall, while Volino *et al.* [24] found the inclination angle on smooth and rough walls agreed within statistical uncertainty.

Raupach *et al.* [25] proposed a wall similarity hypothesis for the outer layer of the rough-wall turbulent flows, as an extension of the Reynolds number similarity of Townsend [26]. It states that the turbulent motions in a boundary layer outside the roughness layer are independent of the wall roughness at a high Reynolds number, which means the effect of surface roughness is confined to the near-wall region. The validity of the wall similarity is extensively investigated since Raupach *et al.* [25]. Some experiments or simulations [18,19,23,27–29] have reported that the roughness effect can be well extended into the outer layer and manifested in the statistics such as the wake strength of the mean velocity profile, while other research provided evidence to support the outer layer similarity [20,24,30–35].

Jimenez [16] proposed that the conflicting views of the wall similarity can be attributed to the different relative heights of the roughness, and estimated that the ratio of the boundary layer thickness to the roughness height should be at least 40 for the wall similarity to be valid. This is

confirmed by the water tunnel experiments of Flack *et al.* [31] and Schultz and Flack [20], the wind tunnel experiments of Squire *et al.* [35], and the field experiments in the atmospheric flow of Kunkel and Marusic [32]. Castro [33] found that the similarity of the mean velocity profile can be maintained with the roughness height up to about  $0.2\delta$  when the Reynolds number is large. The two-dimensional roughness is found to have a larger effect on the outer layer flow, especially on the vertical fluctuation intensity [19,28,36,37]. Krogstad and Efros [22] demonstrated that the outer layer changes induced by the two-dimensional roughness can be significantly reduced when increasing the Reynolds number. Thus the wall similarity hypothesis is proved to be valid for both the two- and three-dimensional roughness, but the restrictions on the Reynolds number and the relative roughness height are different [38]. As noted by Jimenez [16], the validity of the wall similarity is also important for the turbulence modeling in LES where the effect of the small-scale roughness must be modeled.

### B. Constrained large-eddy simulation

The approach of large-eddy simulation (LES) is to capture the fundamental quantities of the turbulent flow by solving the governing equations of a reduced set of modes. Typically the modes of the large-scale motions are resolved and the modes of the small-scale fluctuations are modeled. As described by the decimation theory of Kraichnan [39], the dynamic effect of all other modes on the explicitly followed modes can be represented by the random forcing amplitudes in the Langevin equations by imposing successive constraints of the realizability inequalities and statistical symmetries. The decimation scheme has its advantage in the invariance to random Galilean transformation directly assured by the statistical constraints. Kraichnan and Chen [40] found that the constrained decimation methods can be used for describing the intermittency effects for the nonlinear model systems. She and Jackson [41] applied the statistical constraint on the Euler system to model the homogeneous isotropic turbulence of a very large (infinite) Reynolds number. They found that both the low- and high-order statistics of turbulence are reproduced accurately by a simple constraint derived from the Kolmogorov energy spectrum. Shi *et al.* [42] found that constraining the energy flux in the inertial subrange can effectively improve the accuracy of the conventional eddy viscosity models. Most recently, Biferale *et al.* [43] formulated the constraint using a Lagrangian multiplier in the Navier-Stokes equation. They demonstrated that the range of  $-5/3$  scaling is extended by about one order of magnitude where the anomalous scaling exponents are well captured.

Just like the energy flux for the isotropic turbulence, the Reynolds stress is essentially important for the wall-bounded turbulence. The LES for the wall-bounded turbulence is always troubled by the problem of the log-layer mismatch in the mean velocity profile due to the inaccurate prediction of the Reynolds stress. Chen *et al.* [14] proposed to solve this problem by imposing constraints on the subgrid-scale (SGS) stress in the near-wall region. This CLES approach has a significant advantage over the conventional hybrid RANS/LES method in capturing the small-scale dynamics in the near-wall region (RANS is short for Reynolds-Averaged Navier-Stokes). Xia *et al.* [44] used the CLES approach to simulate the channel flows with the streamwise periodic constrictions, and found that the accurate predictions for this separated flow can be obtained even if the grid is quite coarse. Jiang *et al.* [45] developed the CLES approach for compressible channel flows by imposing constraints on both the SGS stress and the SGS heat flux. Hong *et al.* [46] and Xia *et al.* [47] applied the CLES to study the compressible flow past a circular cylinder. Zhao *et al.* [48] introduced the intermittency factor in the CLES model and applied it to simulate the laminar-turbulent transition process. Chen *et al.* [49] simulated the flow past a full-scale commercial aircraft and demonstrated that the CLES is also a promising tool for the engineering applications.

## III. NUMERICAL METHOD

### A. Constrained SGS stress

Typically in LES the SGS stress ( $\tau_{ij}$ ) is calculated using an eddy-viscosity model with the instantaneous local strain rate, while the mean shear is related to the mean stress. In the framework

of CLES [14],  $\tau_{ij}$  is formulated as

$$\tau_{ij} = \tau_{ij}^m + R_{ij}^m - R_{ij}^{\text{LES}} - \langle \tau_{ij}^m \rangle, \quad (1)$$

where  $\tau_{ij}^m$  is the stress obtained from an eddy-viscosity model,  $R_{ij}^{\text{LES}} = \langle \tilde{u}_i \tilde{u}_j \rangle - \langle \tilde{u}_i \rangle \langle \tilde{u}_j \rangle$  is the resolved Reynolds stress, and  $\tilde{u}_i$  is the resolved velocity in LES.  $R_{ij}^m$  is the artificially prescribed mean stress, with which the preferred mean shear can be achieved. As the mean part and the fluctuation part of the SGS stress are modeled separately, this formulation bridges the gap between the local SGS stress and the mean stress.  $R_{ij}^m$  can be obtained by the mixing length model

$$R_{ij}^m = -l_{\text{mix}}^2 \left| \frac{\partial \langle \tilde{u}_i \rangle}{\partial x_j} \right| \frac{\partial \langle \tilde{u}_i \rangle}{\partial x_j}, \quad (2)$$

where  $l_{\text{mix}}$  is Prandtl's mixing length. As proposed by Chen *et al.* [14], the log-layer mismatch can be eliminated by setting  $l_{\text{mix}}^+ = \kappa y^+ D(y^+)$  in the simulation of smooth-wall flows, where  $D(y^+) = 1 - \exp(y^+/A^+)$  is the van Driest damping function,  $\kappa \approx 0.4$ ,  $A^+ \approx 26$ ; the quantity with "+" has been normalized in viscous scales. So, the mean velocity distribution of  $U^+ = \kappa^{-1} \ln(y^+) + B$  with  $B \approx 5$  can be reproduced in the logarithmic region.

In the rough-wall flows, the mean velocity in the logarithmic region is downward shifted by  $\Delta U^+$ , i.e.,  $U^+ = \kappa^{-1} \ln(y^+) + B - \Delta U^+$ , due to the roughness-modified mean shear.  $\Delta U^+$  is a function of  $k_s^+$ , which is the equivalent height of Nikuradse's sand roughness. To impose such a rough-wall-like mean shear in LES, we can use the following modified formulation of  $l_{\text{mix}}$  [50–53],

$$l_{\text{mix}}^+ = \kappa(y^+ + \Delta y^+) \{1 - \exp[-(y^+ + \Delta y^+)/A^+]\}, \quad (3)$$

so that a certain  $\Delta U^+$  can be obtained by a corresponding  $\Delta y^+$ . We propose the following correlation:

$$\Delta y^+ = 0.017(k_s^+)^2 \left[ 1 + \left( \frac{k_s^+}{15} \right)^{3.5} \right]^{-1.5/3.5} \left[ 1 + \left( \frac{k_s^+}{350} \right)^4 \right]^{0.35/4}, \quad (4)$$

which can fit the experimental data of Nikuradse [1] quite well. Once the mean shear is constrained, we will focus our attention on the response of the wall turbulence.

In CLES of the channel flows, the filtered Navier-Stokes equations are solved using a Fourier-Chebyshev pseudospectral method with the 2/3 truncation rule to dealias the nonlinear term. The implicit second-order Adams-Bashforth scheme is used for time integration. The code has been extensively validated in previous research [14]. For all the cases, the simulation domain is  $(4\pi \times 2 \times 2\pi)h$  ( $h$  is the half channel width) with  $64 \times 65 \times 64$  grid points in the streamwise, wall-normal, and spanwise direction, respectively. The size of the simulation domain is large enough for present simulations [11]. Uniform grid and periodic boundary conditions are used in the streamwise and spanwise directions, and the Chebyshev collocation points are used in the wall-normal direction. The no-slip and no-penetration Dirichlet boundary conditions are used on the planar walls. After the turbulent flow is fully developed, the statistical results are obtained from 500 snapshots of the flow field during five large-eddy-turnover times.

## B. Equilibrium-wall model

Previously several wall models have been proposed to simulate the rough-wall condition in LES, such as the equilibrium-wall model [54] and the integral-wall model [55]. Simulations of the smooth- and rough-wall flows are also carried out using the equilibrium-wall model for comparison. The equilibrium wall model is derived from the logarithmic distribution  $U/u_\tau = \kappa^{-1} \ln(y^+) + B - \Delta U^+$ , which is equivalent to  $U/u_\tau = \kappa^{-1} \ln(y^+/y_0^+)$  with  $y_0^+ = \exp[-\kappa(B - \Delta U^+)]$ . By definition, the kinematic wall stress is  $\tau_w = u_\tau^2$  for incompressible flows with a constant density. Thus the wall stress can be formulated as  $\tau_w = -[\frac{\kappa}{\ln(y^+/y_0^+)}]^2 U^2$ . In the LES with the equilibrium

wall model, the wall stress is explicitly added on the first grid point above the wall with the following formulation:

$$\tau_w = - \left[ \frac{\kappa}{\ln(y^+/y_0^+)} \right]^2 (\tilde{u}^2 + \tilde{w}^2), \quad (5)$$

where  $y_0^+$  is calculated from  $\Delta U^+$ , which is a function of  $k_s^+$ .  $\tilde{u}$  and  $\tilde{w}$  are the local instantaneous streamwise and spanwise velocity, respectively [56]. Typically this model is used with a relatively coarse grid resolution in the near-wall region.

We use the John-Hopkins open-source code LESGO to simulate the channel flow cases with the equilibrium-wall model. The code solves the filtered Navier-Stokes equations with a staggered grid. A pseudospectral approach is used in the wall-parallel directions and a second-order finite-difference scheme is used in the wall-normal direction. The number of grid points and the size of the simulation domain are the same as those used in CLES, except that the grid points in the wall-normal direction are uniformly distributed. The scale-dependent Lagrangian-average dynamic model [56] is used. More details about the code can be found in Bou-Zeid *et al.* [56], and the references therein. The statistics are obtained from 500 snapshots of the flow field during five large-eddy-turnover times after the turbulence is fully developed.

## IV. NUMERICAL TESTS AND RESULTS

### A. Test cases

First we simulated the smooth wall flows ( $k_s^+ = 0$ ) at  $\text{Re}_\tau = 180$  and 590 without any constraint and without the equilibrium-wall model. The grid resolution, the filtering scheme, and the SGS model are checked carefully (see the Appendixes) to ensure the simulation results match the smooth-wall direct numerical simulation (DNS) results [57]. Then the rough-wall-like mean shear corresponding to various  $k_s^+$  ( $k_s^+ = 15, 30$  for  $\text{Re}_\tau = 180$ ,  $k_s^+ = 30, 60$  for  $\text{Re}_\tau = 590$ ) are imposed using the SGS stress formulation of CLES. Independently, the equilibrium-wall model is used to simulate the channel flow at  $\text{Re}_\tau = 590$  with  $y_0^+ = 2.29 \times 10^{-4}$ ,  $1.75 \times 10^{-3}$ , and  $3.86 \times 10^{-3}$  corresponding to  $k_s^+ = 0, 30$ , and 60. The statistical results are as follows.

### B. Mean velocity profile and fluctuation intensity

The mean streamwise velocity distributions obtained from the numerical tests are shown in Fig. 1. In the smooth-wall flows, the velocity profiles match the DNS results very well. The mean velocity matches the linear distribution  $U^+ = y^+$  in the viscous sublayer up to  $y^+ = 5$ . Once the constraint is imposed, the mean velocity deviates from  $U^+ = y^+$  in the viscous sublayer. The downward shift of the mean velocity in the logarithmic and outer layer matches the expected logarithmic law very well as shown in Figs. 1(a) and 1(b). The nondimensional mean shear is smaller in the near-wall region for rough-wall flows than in smooth-wall flows.

In the cases simulated using the equilibrium-wall model, the mean velocity at the first grid point matches the expected logarithmic law as shown in Fig. 1(c), which means the model functions correctly. However, in the outer layer the result is not accurate. This is caused by the relatively small wall distance of the first grid point. It demonstrates a drawback of the equilibrium-wall model which requires that the first grid point is located in the logarithmic region. But generally, the downward shift of the velocity profile for different  $k_s^+$  is well presented by the equilibrium-wall model.

The velocity fluctuation intensities are shown in Fig. 2. In the simulation of the smooth-wall flows the streamwise fluctuation intensities in the smooth-wall flows match the DNS results quite well. It should be noted that neither the mean shear constraint nor the equilibrium-wall model is used in the smooth-wall cases. Once the rough-wall-like mean shear is imposed, the peak fluctuation intensity of streamwise velocity decreases significantly, while in the spanwise and wall-normal directions the peak fluctuation intensities remain almost unchanged at both  $\text{Re}_\tau = 180$  and  $\text{Re}_\tau = 590$  as shown in Figs. 2(a) and 2(b). This phenomenon is consistent with the DNS results of Yuan and Piomelli [58].

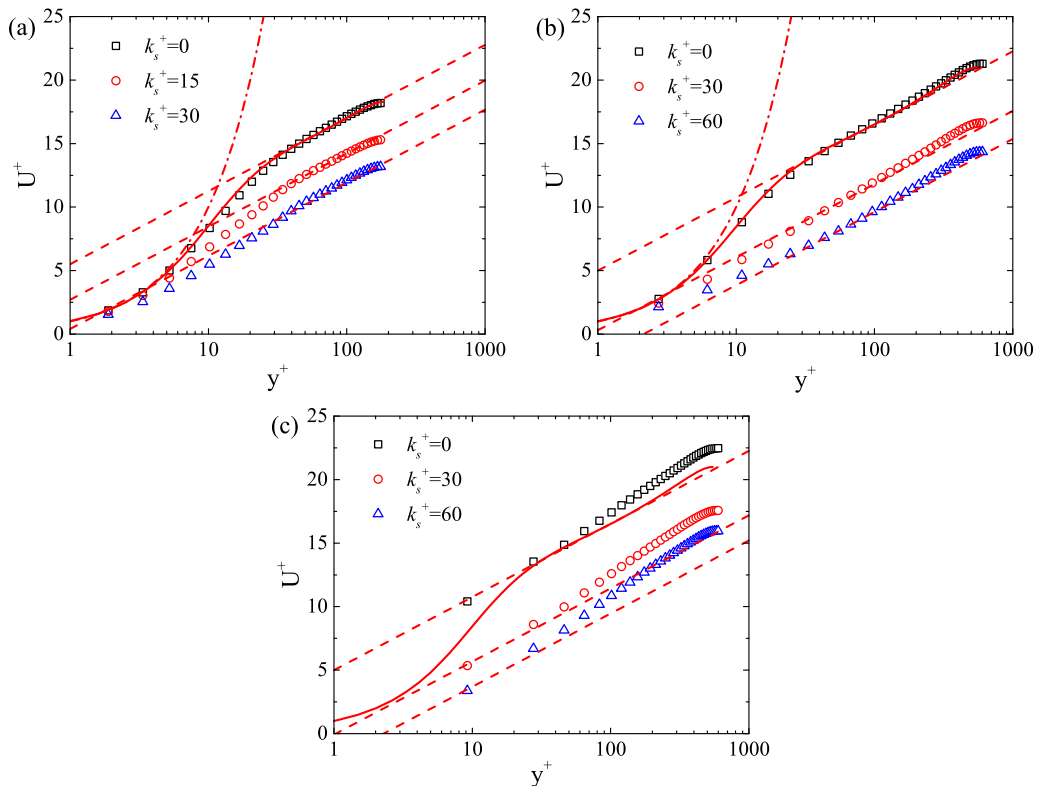


FIG. 1. (a),(b) Mean streamwise velocity profile of the channel flows at  $Re_\tau = 180$ ,  $Re_\tau = 590$ ; the mean shear constraint is imposed for the cases of  $k_s^+ > 0$ . (c) The mean velocity profile obtained from the simulation with the equilibrium-wall model at  $Re_\tau = 590$ . The solid lines are the DNS results of the smooth-wall flows at  $Re_\tau = 180$  and  $550$  [57]. The dashed lines are the expected logarithmic distribution  $U^+ = \kappa^{-1} \ln(y^+) + B - \Delta U^+$  for each case. The dash-dotted lines represent the linear distribution  $U^+ = y^+$ .

As shown in Fig. 2(c), when the equilibrium-wall model is used, the peak fluctuation intensities are underestimated in the near-wall region due to the insufficient grid resolution there. But the decrease of the streamwise fluctuation intensities is also observed when  $k_s^+$  increases.

In experiments it is found that the flow will be displaced away from the wall by the surface roughness due to the blockage in the near-wall region [59]. In the DNS of Yuan and Piomelli [58], the outward shift of the position of the peak fluctuation intensities is observed. But this effect is less significant when only the mean shear is imposed, as the blockage effect of roughness element is not fully introduced.

The collapse of the fluctuation intensities in the outer layer for different  $k_s^+$  is observed at each  $Re_\tau$  in Fig. 2, which identifies the outer layer similarity. This is related to the outer layer similarity of the mean streamwise velocity since the production of the turbulent kinetic energy is the same in the outer layer for different  $k_s^+$ . It also indicates the imposed mean-shear-constraint functions just like the stress boundary condition in the equilibrium-wall model.

It should be stressed that the effect of roughness elements is not limited to change of the mean shear. As shown by Bhaganagar and Chau [60], the fluctuation intensities in the outer layer depend on the detailed roughness geometry. The outer layer similarity only exists when the roughness is random and irregular, but the similarity is destroyed by the idealized regular roughness. Ikeda and Durbin [61] found that a high-energy region is formed by the strong motions just above the transverse rectangular ribs, and the vortical structures are responsible for the high-energy

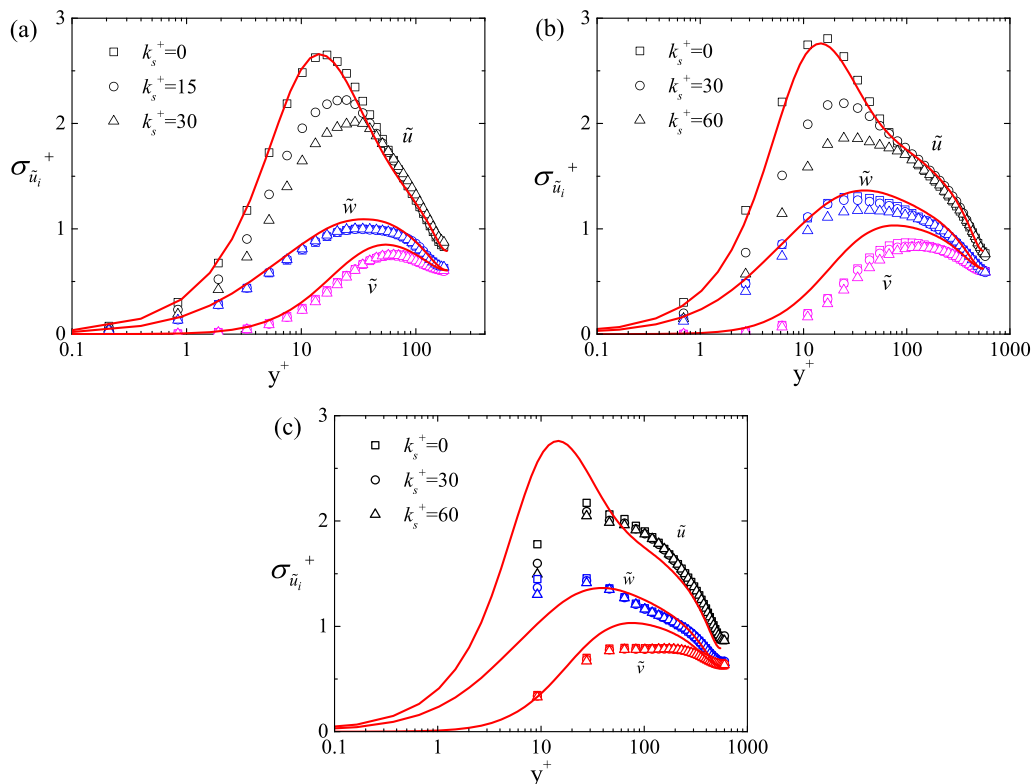


FIG. 2. (a),(b) The distribution of the velocity fluctuation intensities of the channel flows at (a)  $Re_\tau = 180$  and (b)  $Re_\tau = 590$ ; the mean shear constraint is imposed for the cases of  $k_s^+ > 0$ . (c) The fluctuation intensities obtained from the simulation using the equilibrium wall model at  $Re_\tau = 590$ . The solid lines are the DNS results of the smooth-wall channel flow at  $Re_\tau = 180$  and  $Re_\tau = 550$ , respectively [57].

production. However, that is not observed in present simulations. Thus, it specifically indicates that the effect of random irregular roughness can be reproduced by imposing the rough-wall-like mean shear uniformly.

### C. Stress budget

The constrained SGS stress can be observed directly from the stress budget. The mean stress distributions of the channel flow at  $Re_\tau = 180$  with and without the constraint on the mean shear are shown in Fig. 3. The total stress decreases linearly as predicted by the integration of the mean momentum equation [26]. The viscous stress decreases very quickly as the wall distance increases. In most parts of the channel the flow is dominated by the resolved Reynolds stress  $(-\langle \tilde{u}\tilde{v} \rangle^+)$ , while the contribution of the SGS stress is mostly concentrated in the near-wall region where the constraint is imposed. In the smooth-wall case ( $k_s^+ = 0$ ) shown in Fig. 3(a), the peak of the SGS stress is about 0.13, which is much smaller than the resolved Reynolds stress. In the cases with the constraint, the SGS stress in the near-wall region is significantly increased, as shown in Figs. 3(b) and 3(c). The peak value of the SGS stress is increased to about 0.38 for  $k_s^+ = 15$  and to about 0.5 for  $k_s^+ = 30$ . That makes the SGS stress even larger than the resolved Reynolds stress in the near-wall region. In the unconstrained outer layer the SGS stress quickly decreases to the level of the viscous stress. A similar phenomenon can be observed from the stress budgets of  $Re_\tau = 590$ .



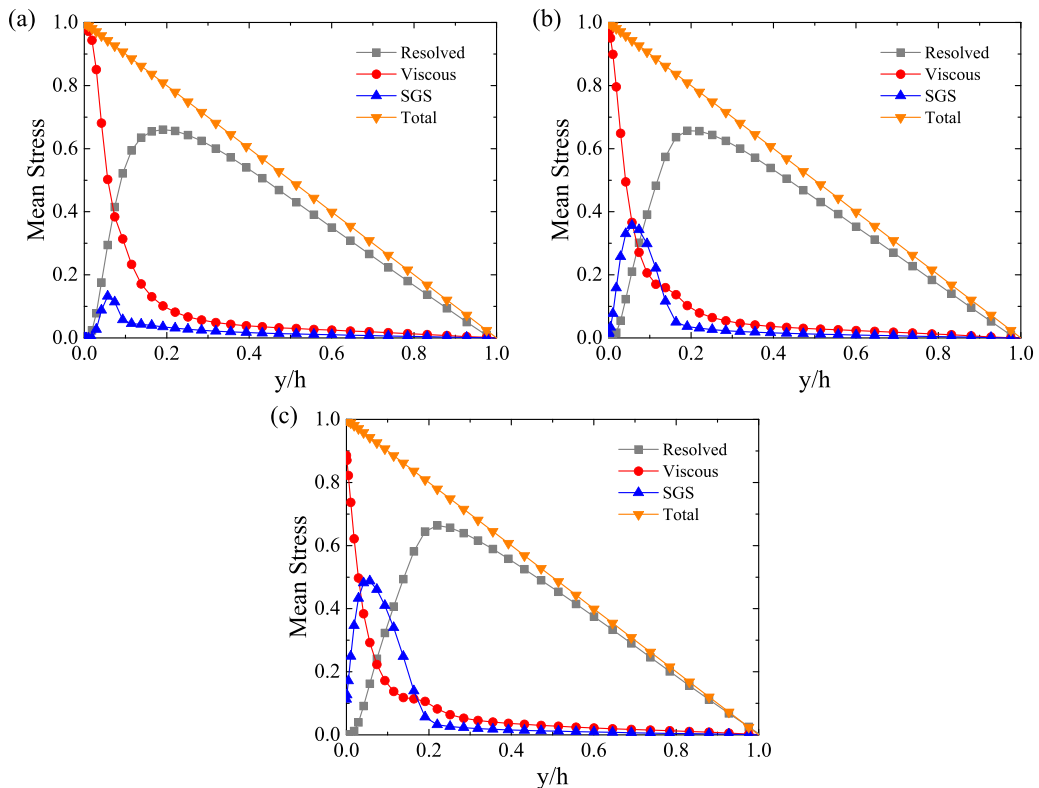


FIG. 3. Mean stress distribution for the channel flows at  $Re_\tau = 180$ , (a)  $k_s^+ = 0$ , (b)  $k_s^+ = 15$ , and (c)  $k_s^+ = 30$ . The mean shear constraint is imposed for the cases of  $k_s^+ > 0$ .

#### D. Spectrum

The spectra of the streamwise velocity fluctuation across the channel are shown in Fig. 4. The spectra are normalized using the wall distance to contrast the different scaling behavior at different scales (see, e.g., [56,62]). Generally in the production range ( $k_u y < 1$ ) the spectrum is expected to have a slope of  $-1$ , and in the inertial subrange ( $k_u y > 1$ ) the energy cascade follows the Kolmogorov spectrum with a slope of  $-5/3$  [56].

For the  $Re_\tau = 180$  cases in Figs. 4(a) and 4(c), the  $k_u^{-1}$  regime at low wave number is clearly observed. Due to the relatively low Reynolds number, the large energy-containing scales and the small dissipative scales are not well separated. Both the  $k_u^{-1}$  and the  $k_u^{-5/3}$  regimes are observed in the  $Re_\tau = 590$  cases as shown in Figs. 4(b) and 4(d). This indicates that the dissipation of the turbulence has been properly modeled in the constrained cases. This is consistent with the correctly predicted fluctuation intensities in the unconstrained smooth-wall cases.

The downward shift of the spectrum in the near-wall region is observed for the constrained cases at both  $Re_\tau = 180$  and 590 comparing the smooth-wall spectrum. This is consistent with the decrease of the near-wall fluctuation intensity shown in Fig. 2. In the outer layer, the spectra are very similar for the smooth- and rough-wall cases, which also indicates the outer layer similarity for the turbulence structure.

#### E. Quadrant analysis

The velocity fluctuations which form the Reynolds stress can be categorized into four types: Q1 ( $u' > 0, v' > 0$ ), Q2 ( $u' < 0, v' > 0$ ), Q3 ( $u' < 0, v' < 0$ ), and Q4 ( $u' > 0, v' < 0$ ) [63]. Q2 and Q4



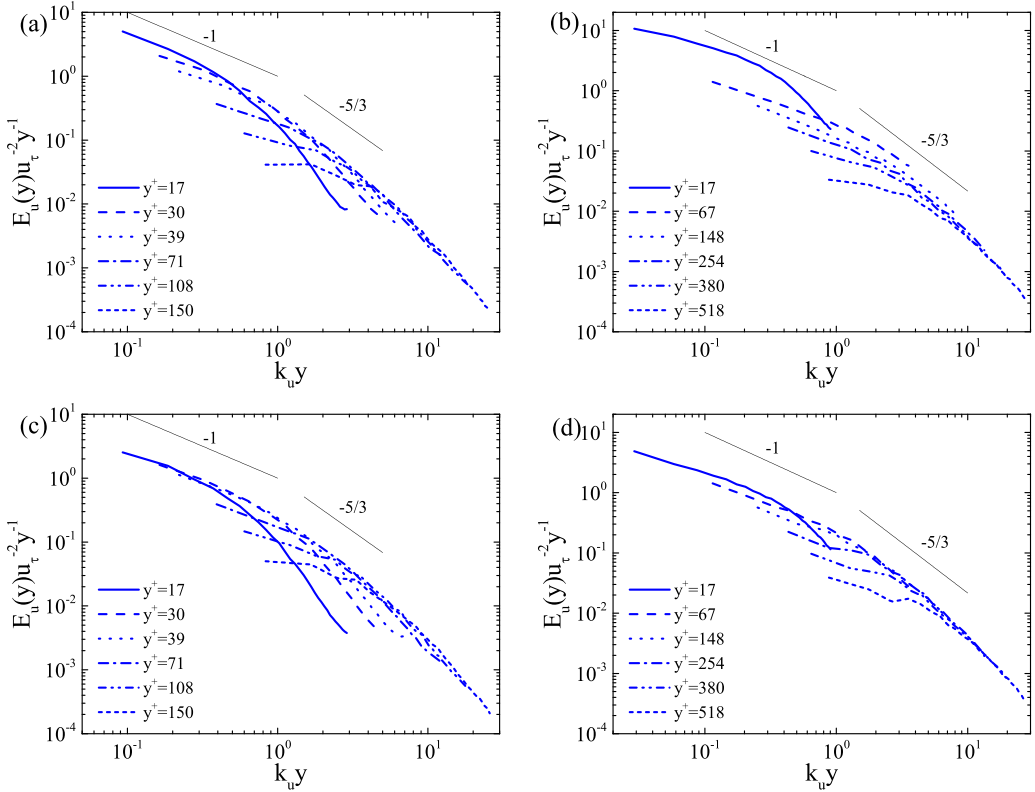


FIG. 4. The normalized spectrum of the streamwise velocity fluctuation obtained from the smooth-wall cases at (a)  $Re_\tau = 180$  and (b)  $Re_\tau = 590$ , and the mean-shear-constrained cases (c)  $Re_\tau = 180$ ,  $k_s^+ = 30$  and (d)  $Re_\tau = 590$ ,  $k_s^+ = 60$ .

motions are directly related to the ejection and sweep events, respectively. Q1 and Q3 are referred to as the outward and inward interactions. Previously it is found that the normalized contribution of Q4 (sweep) to the Reynolds stress is enhanced in the near-wall region due to the surface roughness [5,17,20,22]. Here we check if this phenomenon can be captured from the resolved flow field by imposing the rough-wall-like mean shear.

Representatively, the joint probability distribution function  $P(u', v')$  and its covariance integrand  $u'v'P(u', v')$  obtained from the simulations at  $Re_\tau = 590$  with and without the constraint are shown in Fig. 5. The statistics are obtained from the resolved flow field and the tilde is neglected for convenience in the following discussion. Three wall-normal locations ( $y^+ = 17, 68, 148$ ) are selected to contrast the statistics in the buffer layer, the logarithmic layer, and the center region of the turbulence. Typically the Q2 and Q4 events have a larger contribution to the Reynolds stress. Thus the  $P(u', v')$  distribution is close to an ellipse, of which the major axis is inclined in the direction of Q2 and Q4 as shown in Figs. 5(a)–5(c). The  $P(u', v')$  obtained in the outer layer ( $y^+ = 148$ ) is very close for the smooth and constrained cases. At  $y^+ = 68$ , the contours of  $P(u', v')$  for the smooth and constrained flows are still very close, but differences can be observed from the contours of  $u'v'P(u', v')$  in Fig. 5(e). The contribution of the intensive  $(u', v')$  fluctuation is decreased. This is related to the fluctuation intensity suppressed in the near-wall region on the rough wall. In Fig. 5(c) the distribution of  $P(u', v')$  at  $y^+ = 17$  is much flattened as the wall-normal fluctuation is obviously suppressed in the near-wall region, while the difference between the smooth and constrained cases should be attributed to the change in the streamwise velocity fluctuation. The

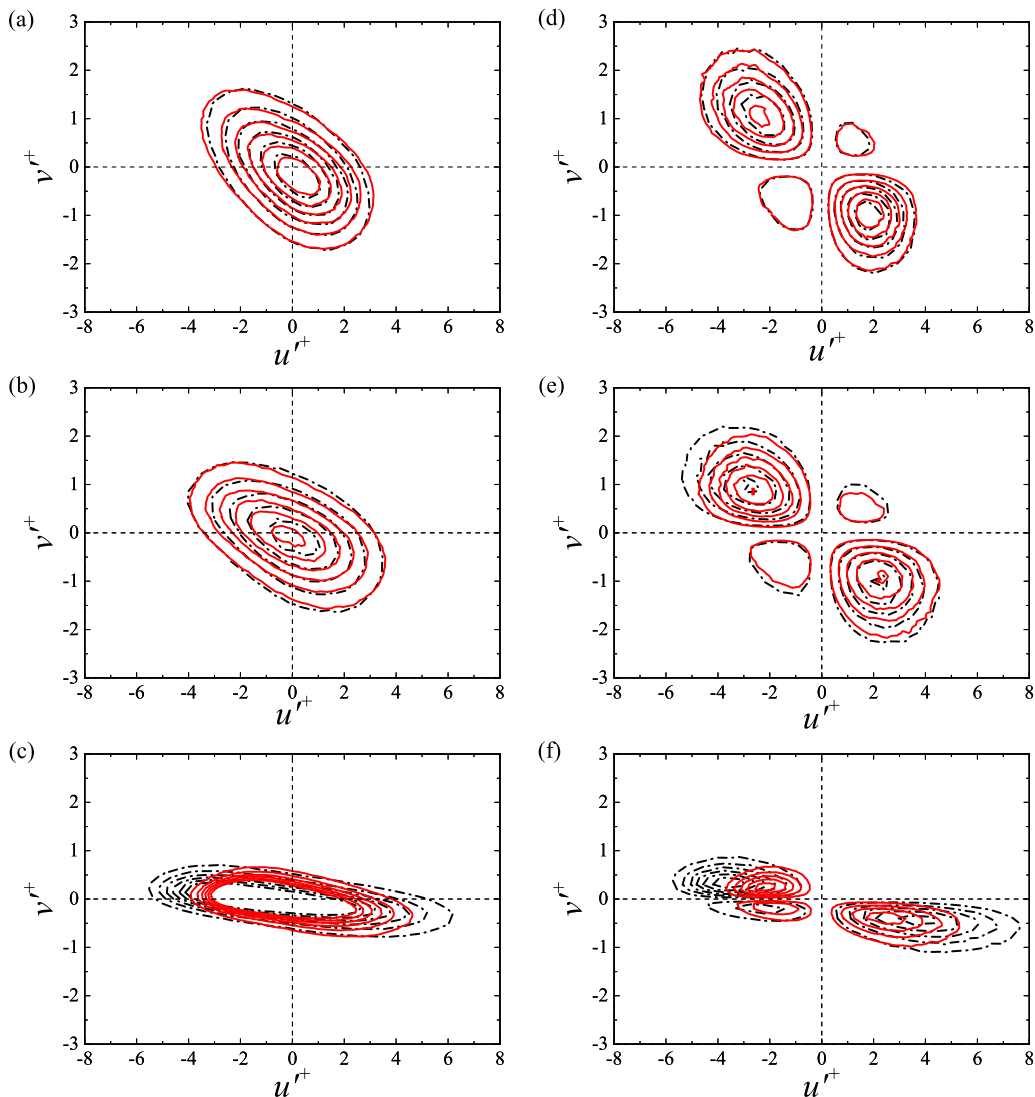


FIG. 5. (a)–(c) The joint probability distribution function  $P(u', v')$ , and (d)–(f) the covariance integrand  $u'v'P(u', v')$  at  $\text{Re}_\tau = 590$ ,  $k_s^+ = 0$  (black dash-dotted contour lines) and  $k_s^+ = 60$  (red solid contour lines) at wall distances of (a),(d)  $y^+ = 148$ , (b),(e)  $y^+ = 68$ , and (c),(f)  $y^+ = 17$ . Contour levels are from 0.0005 to 0.003 for (a)–(c) and from  $-0.003$  to 0.001 for (d)–(f) with the same contour spacing 0.0005.

Q2 and Q4 contributions to the Reynolds stress are also significantly reduced on the rough wall as shown in Fig. 5(f).

The quadrant contribution normalized by the resolved Reynolds stress is shown in Fig. 6(a). Q2 and Q4 events provide the major contribution. The resolved Reynolds stress is dominated by the Q4 contribution in the near-wall region and by the Q2 contribution in the outer layer, which is consistent with the general knowledge of the momentum flux in wall turbulence. Comparing to the smooth-wall flow, it can be observed that the Q4 contribution increases in the near-wall region ( $y^+ \leq 50$ ) of the constrained flow. The Q2 contribution slightly decreases and the Q3 contribution increases to balance the change of the Q4 contribution, which also indicates the fluid motions towards the wall

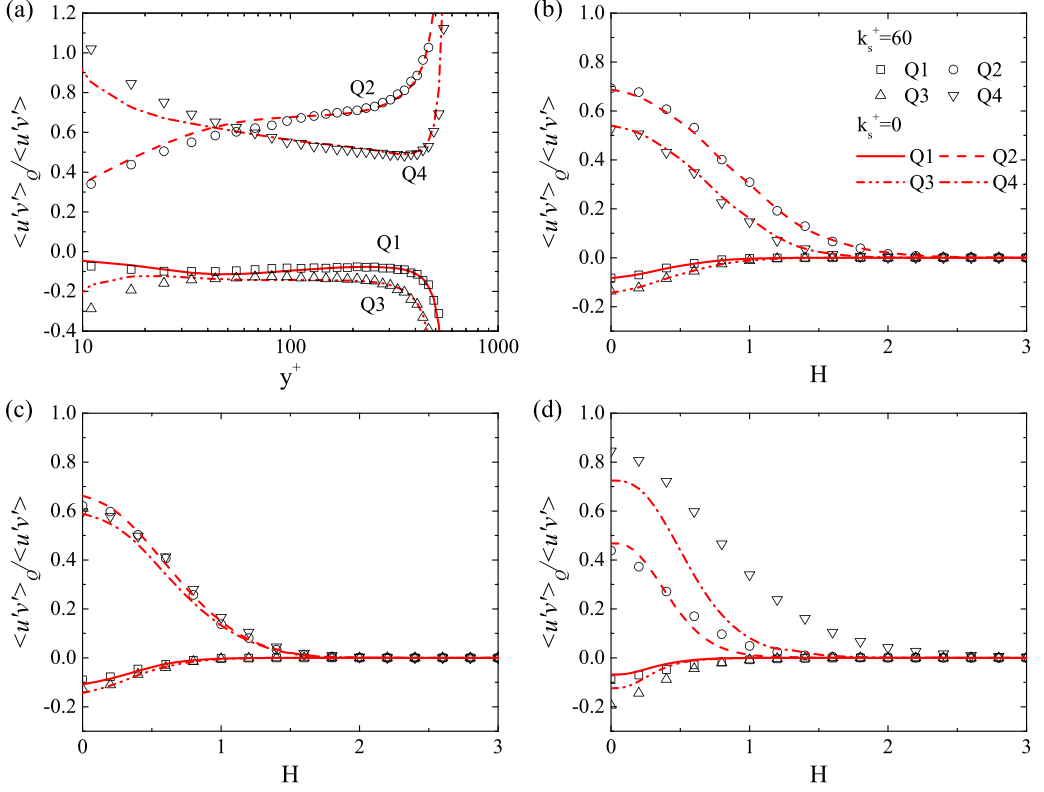


FIG. 6. (a) Quadrant contributions of the resolved Reynolds stress throughout the channel at  $Re_\tau = 590$  in the smooth-wall case (lines: solid, Q1; dashed, Q2; dash-dot-dotted, Q3; dash-dotted, Q4) and the constrained case ( $k_s^+ = 60$ ; square, Q1; circle, Q2; up triangle, Q3; down triangle, Q4). Fractional quadrant contributions of the resolved Reynolds stress filtered by the hyperbolic hole at wall-normal distances of (b)  $y^+ = 148$ , (c)  $y^+ = 68$ , and (d)  $y^+ = 17$ . Lines and symbols are consistent with (a).

are enhanced. It should be noted that in LES, the fluctuation of small-scale turbulence has been filtered out, which makes the increase of normalized Q4 contribution less significant. It will be shown in Fig. 16 in Appendix B that the increase of the normalized Q4 contribution is more evident when more grid points are used.

With the concept of a hyperbolic hole [64], the filtered contribution of each quadrant is defined by

$$\langle u'v' \rangle_Q(H) = \iint [u'v'P(u', v')]_Q I(H) du' dv', \quad (6)$$

where  $I(H)$  is the indicator function:

$$I(H) = \begin{cases} 1 & \text{when } |u'v'| > H \langle u'v' \rangle \\ 0 & \text{otherwise.} \end{cases} \quad (7)$$

This filtering operation with the parameter  $H$  can be used to separate the contribution of quadrant events of different strengths.

The filtered quadrant contribution of the rough-wall flow is compared with that of the smooth-wall flow in Figs. 6(b)–6(d). At  $y^+ = 148$ , the smooth and constrained results are almost the same as shown in Fig. 6(b). At  $y^+ = 68$  as shown in Fig. 6(c), the Q4 contribution increases slightly

within the range  $0 < H < 1.5$ , and the Q2 contribution decreases very slightly within  $H < 0.5$ . At  $y^+ = 17$  as shown in Fig. 6(d), the increase of the Q4 contribution is evident, and the largest change occurs around  $H = 1$ . It indicates that the increase of the Q4 contribution consists of more strong sweep events. Note that the Q2 contribution slightly decreases within  $H < 0.4$  and increases within  $0.4 < H < 1.5$ . This means that the ejection events with strength around  $H = 1$  occur slightly more frequently, but that is compensated by a greater loss caused by the decrease of weaker ejection. The Q3 contribution also increases slightly within  $H < 0.7$ , which is probably linked to the increase of strong Q4 events since both Q3 and Q4 motions are towards the wall.

The wall similarity is identified from the quadrant analysis in the outer layer and the increase of the normalized Q4 contribution to the resolved Reynolds stress is observed in the constrained flow. It indicates the near-wall constraint on the mean shear acts just like the rough-wall condition, as observed in previous experiments of rough-wall flows, (e.g., Raupach [17], Schultz and Flack [20], Krogstad and Efros [22]).

## F. Two-point correlation

Finnigan [6] argued that the increase of the normalized Q4 (sweep) contribution is attributed to the formation of the stronger correlational vortex structures, which typically consist of a pair of counter-rotating streamwise vortices, and the strong sweep is generated between the vortex pair. Krogstad and Antonia [23] found a significant increase in the inclination angle of the correlational structure in rough-wall flows, while the later experiments of Volino *et al.* [24] indicates the inclination angle is unchanged considering the experimental uncertainty. Since the increase in the normalized contribution of the Q4 event to the Reynolds stress has been observed in the present simulations, we further check the turbulence structure in the resolved flow field with the two-point correlation of the streamwise velocity.

In the  $(x, y)$  plane, the two-point correlation  $\rho_{uu}$  is defined as

$$\rho_{uu}(\Delta x, y, y_{\text{ref}}) = \frac{\langle u'(x, y_{\text{ref}}, z)u'(x + \Delta x, y, z) \rangle}{\sigma_u(y_{\text{ref}})\sigma_u(y)}, \quad (8)$$

where  $\sigma_u$  is the streamwise velocity fluctuation intensity. For each reference wall-normal location  $y_{\text{ref}}$ , the correlation is calculated with various  $y$  and  $\Delta x$ , averaged in time and in the horizontal plane, and then normalized with the fluctuation intensities at  $y_{\text{ref}}$  and  $y$ .

The two-point correlations in the  $(x, y)$  plane of the simulation results of the smooth-wall and the constrained cases at  $\text{Re}_\tau = 590$  are shown in Fig. 7. Generally a larger and stronger correlational structure is observed in the constrained case comparing to that in the smooth-wall flow. As shown in Figs. 8(a) and 8(d), with  $y_{\text{ref}}^+ = 148$  the contour line for  $\rho_{uu} = 0.2$  extends from  $\Delta x/h = -1.5$  to 1.75 in the streamwise direction in the smooth-wall case, and extends from about  $\Delta x/h = -2.2$  to about 1.9 in the constrained case. As  $y_{\text{ref}}^+$  decreases to 68 in Figs. 8(b) and 8(e), the size of the correlation structure reduces, which makes the difference between the structure on the smooth-wall case and the constrained case even more evident. With  $y_{\text{ref}}^+ = 17$  in Figs. 8(c) and 8(f), the contour line for  $\rho_{uu} = 0.2$  extends to  $\Delta x/h = 0.25$  on the rough wall, but only to  $\Delta x/h = 0.12$  on the smooth wall. This phenomenon is consistent with the increase of the normalized Q4 contribution in rough-wall flows [6].

The inclination angle of the mean vortex structure can be determined from the contour lines of the two-point correlation. The farthest point of each contour level  $\rho_{uu} = (0.3, 0.4, 0.5)$  is used to identify the major axis of the inclined ellipse. Note that we do not use a contour level of a larger  $\rho_{uu}$  as many researchers did (e.g., [24,65]), because in the present simulations the grid spacing is relatively large so that the contour line for a larger correlation value does not have a smooth ellipselike shape. It is found that the inclination angles at  $y_{\text{ref}}^+ = 17, 68,$  and  $148$  are about  $5.7^\circ, 9.9^\circ,$  and  $12.9^\circ$  on the smooth wall, and  $10.9^\circ, 10.2^\circ,$  and  $12.6^\circ$  on the rough wall, as marked in Fig. 8 with the inclined solid lines. In the outer layer the inclination angle is in excellent agreement with Heisel *et al.* [65] and Adrian *et al.* [66], and very close in both the smooth-wall case and the

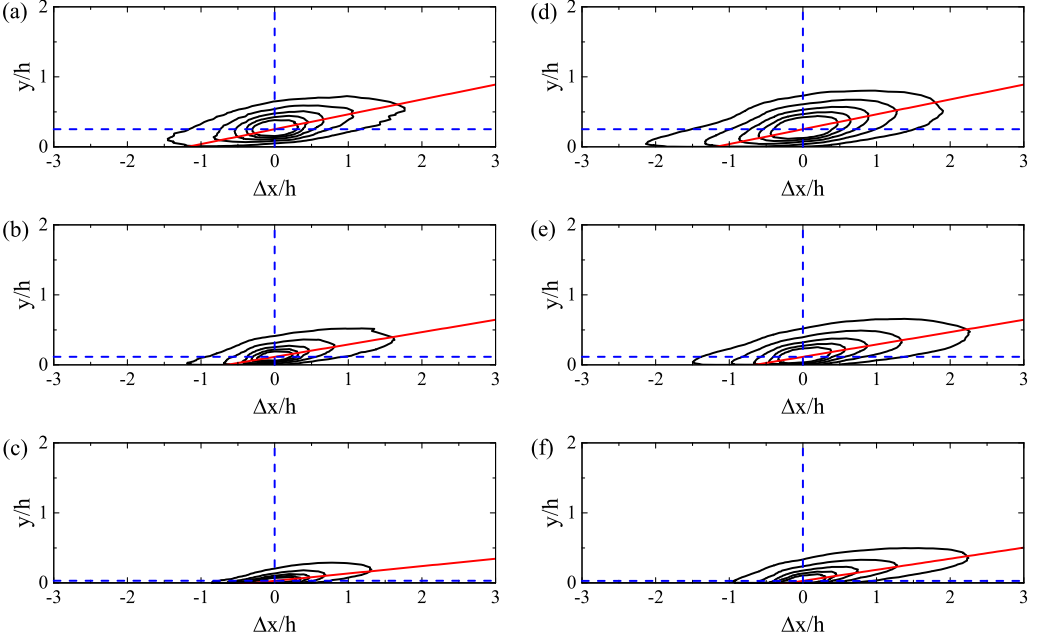


FIG. 7. Two-point correlations of the streamwise fluctuation velocity at  $Re_\tau = 590$ , (a)–(c) smooth and (d)–(f) constrained ( $k_s^+ = 60$ ), with the reference wall distance of (a),(d)  $y_{ref}^+ = 148$ , (b),(e)  $y_{ref}^+ = 68$ , and (c),(f)  $y_{ref}^+ = 17$ . The contour levels are (0.2, 0.3, 0.4, 0.5, 0.6) from the outside to the inside. The straight solid line (red) is inclined to show the inclination angle of the correlational structure.  $y_{ref}^+$  is represented by the horizontal dashed line.

constrained case. A larger inclination angle is only observed in the near-wall region, but is much less significant than the increase reported by Krogstad *et al.* [18].

The two-point correlation in the  $(y, z)$  plane shown in Fig. 8 is defined as

$$\rho_{uu}(y, \Delta z, y_{ref}) = \frac{\langle u(x, y_{ref}, z)u(x, y, z + \Delta z) \rangle}{\sigma_u(y_{ref})\sigma_u(y)}. \quad (9)$$

Typically in the  $(y, z)$  plane a region of positive correlation around the reference point is accompanied by two negative correlation regions on both sides. In a sense of statistical average, the downward sweep motion is generated between the vortex pair and the upward ejection motion occurs on the outer side of the vortex pair.

In the constrained case shown in Figs. 8(d)–8(f), the area of positive correlation with  $\rho_{uu} = 0.05$  extends up to the center region of the channel. A strong negative correlation  $\rho_{uu} = -0.175$  is achieved when  $y_{ref}^+ = 148$  and the boundary of the negative correlation area becomes much smoother. The level of negative correlation  $\rho_{uu} = -0.1$  is still observable when  $y_{ref}^+ = 68$  as shown in Fig. 9(e). Even when the reference wall distance is reduced to  $y_{ref}^+ = 17$ , a relatively large area of negative correlation ( $\rho_{uu} = -0.05$ ) can be observed, and the near-wall flow has a weak positive correlation with the flow close to the channel center ( $y/h \approx 0.8$ ), as shown in Fig. 9(f). In the smooth-wall flow in Figs. 9(a)–9(c) the area of positive correlation is smaller than that in the rough-wall flow at each level, and the difference is even more evident in the negative correlation area. As  $y_{ref}^+$  decreases from 148 to 17, the area of negative correlation (e.g.,  $\rho_{uu} = -0.05$ ) reduces very quickly. The differences of the two-point correlation in the  $(y, z)$  plane indicate that stronger correlational structures are formed in the rough-wall flow. This is consistent with the findings in the quadrant statistics and the two-point correlation in the  $(x, y)$  plane.

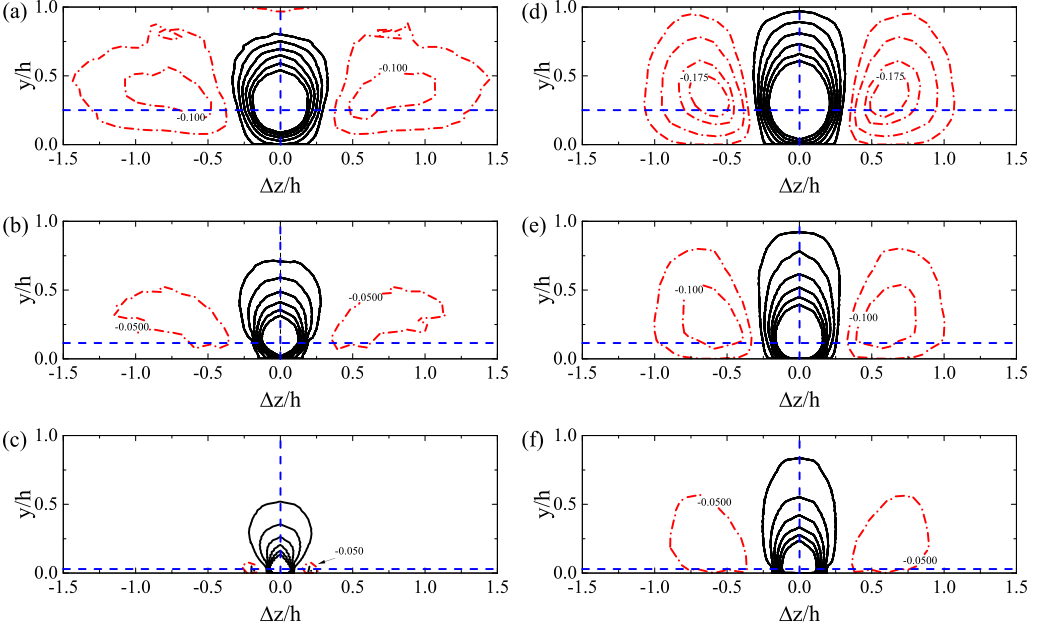


FIG. 8. Two-point correlations of the streamwise fluctuation velocity in the  $(y, z)$ -plane at  $Re_\tau = 590$ , (a)–(c) smooth wall, (d)–(f) constrained ( $k_s^+ = 60$ ) with the reference wall distances of (a),(d)  $y_{\text{ref}}^+ = 148$ , (b),(e)  $y_{\text{ref}}^+ = 68$ , (c),(f)  $y_{\text{ref}}^+ = 17$ . The contour levels for the positive correlation are plotted from 0.05 to 0.3 with the contour spacing of 0.05. The negative contour levels ( $-0.175, -0.15, -0.1, -0.05$ ) are plotted if they exist.  $y_{\text{ref}}^+$  is represented by the horizontal dashed line.

The two-point correlations obtained from the simulation with the equilibrium-wall model are shown in Fig. 9 for comparison. The difference of  $\rho_{uu}$  in the  $(y, z)$  plane obtained for different  $k_s^+$  are also very significant. This can be observed from the peak value of the negative  $\rho_{uu}$ . Specifically,

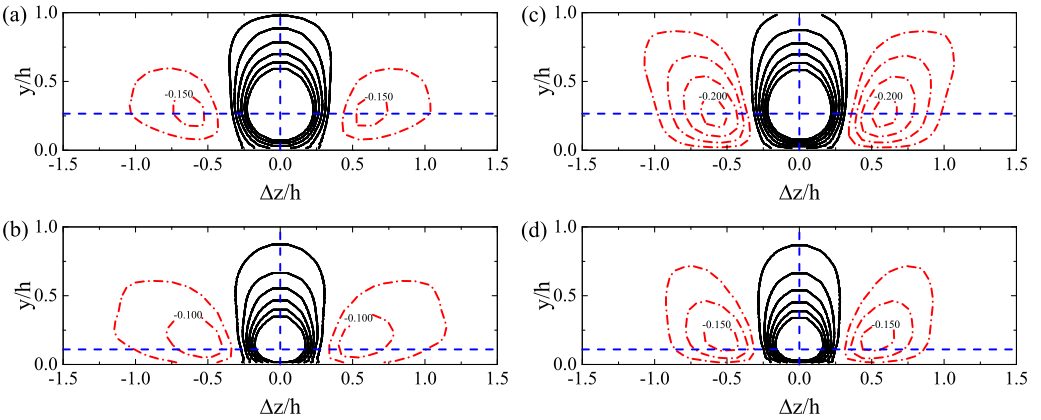


FIG. 9. Two-point correlations of the streamwise fluctuation velocity in the  $(y, z)$  plane obtained from the simulations using the equilibrium-wall model at  $Re_\tau = 590$ , with (a),(b)  $k_s^+ = 0$  and (c),(d)  $k_s^+ = 60$  with the reference wall distances of (a),(c)  $y_{\text{ref}}^+ = 157$ , (b),(d)  $y_{\text{ref}}^+ = 65$ . The contour levels for the positive correlation are plotted from 0.05 to 0.3 with the contour spacing of 0.05. The negative contour levels ( $-0.2, -0.15, -0.1, -0.05$ ) are plotted if they exist.  $y_{\text{ref}}^+$  is represented by the horizontal dashed line.

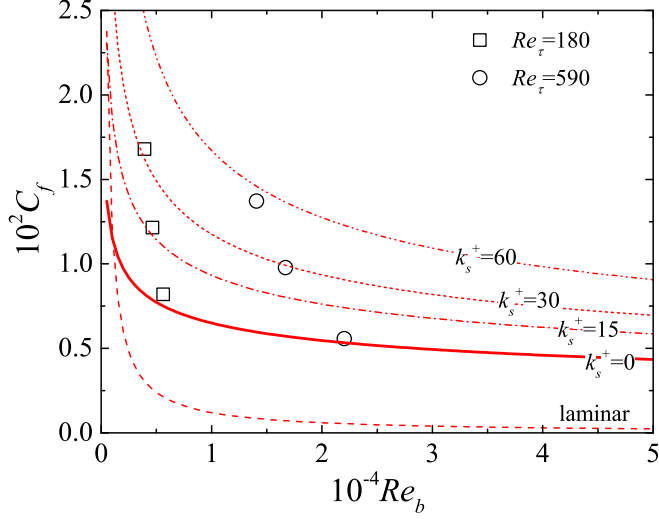


FIG. 10. Total skin friction coefficient obtained from the present LES using the decomposition (open symbols). The correlation function for the smooth-wall flows is  $C_f = 0.065\text{Re}_b^{-0.25}$  (thick solid line), and for laminar flow is  $C_f = 12/\text{Re}_b$  (dashed line). The correlation for other  $k_s^+$  is derived from (15).

in the  $k_s^+ = 0$  case the negative  $\rho_{uu}$  reaches  $-0.15$  and  $-0.1$  with  $y_{\text{ref}}^+ = 157$  and  $65$ , respectively. In the  $k_s^+ = 60$  case the negative  $\rho_{uu}$  is increased to  $-0.2$  and  $-0.15$  with corresponding  $y_{\text{ref}}^+$ . Thus the correlational structure is stronger, which is consistent with the simulation results obtained by constraining the mean shear.

### G. Skin friction coefficient

Generally, the skin friction will be increased due to the surface roughness. In this section, we use the Fukagata-Iwamoto-Kasagi, decomposition proposed by Fukagata *et al.* [67] to illustrate that imposing the rough-wall-like mean shear also introduces additional drag force to the turbulent flow, which is similar to the effect of the surface roughness.

The skin friction coefficient ( $C_f$ ) is defined by

$$C_f = \frac{\tau_w^*}{\frac{1}{2}\rho^*U_b^{*2}} = \frac{2}{U_b^{+2}}, \quad (10)$$

where the superscript “\*” represents the quantity is dimensional,  $\tau_w$  is the friction stress on the wall, and the bulk velocity ( $U_b^+$ ) is defined by

$$U_b^+ = \frac{1}{h} \int_0^h U^+ dy. \quad (11)$$

Following the method proposed by Fukagata *et al.* [67], the decomposition of the skin friction coefficient can be obtained:

$$C_f = \frac{12}{\text{Re}_b} + \underbrace{\frac{6}{U_b^{+2}} \int_0^1 \left(1 - \frac{y^+}{h^+}\right) (-\langle \tilde{u}'\tilde{v}' \rangle^+) dy^+}_{\text{Resolved}} + \underbrace{\frac{6}{U_b^{+2}} \int_0^1 \left(1 - \frac{y^+}{h^+}\right) (-\langle \tau_{12} \rangle^+) dy^+}_{\text{SGS}}, \quad (12)$$

where  $\text{Re}_b$  is the bulk Reynolds number defined by

$$\text{Re}_b = \frac{2U_b^* h^*}{\nu^*}, \quad (13)$$



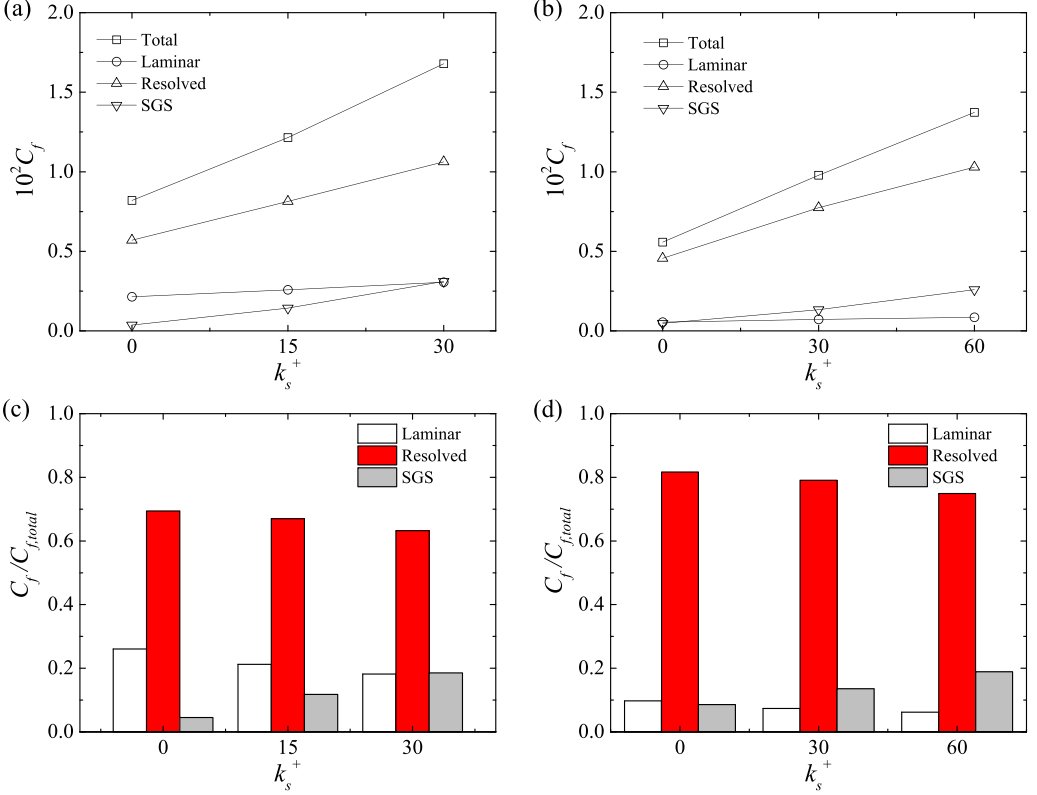


FIG. 11. (a),(b) Skin friction coefficient obtained from the decomposition and (c),(d) the percentage contribution of the laminar part, the resolved turbulent part, and the SGS part, at (a),(c)  $Re_\tau = 180$  and (b),(d)  $Re_\tau = 590$ .

and it can be derived that  $Re_b = 2U_b^+ Re_\tau$ . The skin friction coefficient is separated into the contributions of the laminar viscous stress ( $12/Re_b$ ), the resolved Reynolds stress, and the SGS stress.

The total skin friction coefficient obtained from the decomposition is shown in Fig. 10. The present simulation results for smooth-wall flows are well fitted by

$$C_f \approx 0.065 Re_b^{-0.25}, \quad (14)$$

which is slightly lower than the experimental correlation of Dean [68]. This is similar to the recent DNS results of Cheng *et al.* [69]. Then  $C_f$  for other  $k_s^+$  can be derived from the following equation:

$$(U_b^+)_{smooth} - (U_b^+)_{rough} = \frac{1}{\sqrt{\frac{1}{2}(C_f)_{smooth}}} - \frac{1}{\sqrt{\frac{1}{2}(C_f)_{rough}}}. \quad (15)$$

As shown in Fig. 11, the total  $C_f$  of the flow with the constraint obtained from (12) is in good agreement with the estimation of (15).

The contribution of each part to the skin friction can be separated as shown in Figs. 11(a) and 11(b). In the constrained cases, the skin friction of the SGS stress and the resolved turbulent stress increases evidently at both  $Re_\tau = 180$  and  $Re_\tau = 590$  comparing to the smooth-wall cases without constraint. Although the downward shift of the mean velocity profile results in the decrease of  $Re_b$ , the increase of the laminar contribution is almost negligible.

The percentage of each part in the total skin friction is shown in Figs. 11(c) and 11(d). At  $Re_\tau = 180$  the contribution of the resolved turbulent stress accounts for about 70% in the smooth-

wall flow and decreases slightly when the rough-wall-like mean shear is constrained. When  $k_s^+ = 0$  the laminar contribution accounts for as much as 26% of the total skin friction, which is much larger than the SGS contribution. When the constraint is imposed for cases with  $k_s^+ > 0$ , the SGS contribution increases, while the laminar contribution decreases to the same level with the SGS contribution when  $k_s^+ = 30$ . At  $Re_\tau = 590$  as shown in Fig. 11(d), the contribution percentage of the resolved turbulent stress is even larger, up to around 80%. The laminar contribution is much smaller comparing to the  $Re_\tau = 180$  case. The SGS contribution can be close to 20% when  $k_s^+$  increases to 60. Generally the constraint of the rough-wall-like mean shear provides extra resistance just like the surface roughness.

## V. DISCUSSION

The turbulent kinetic energy (TKE) production in the turbulent flow over rough walls is very complicated for both the regular roughness (see, e.g., Ikeda and Durbin [61]) and the irregular roughness (see, e.g., Yuan and Piomelli [58]). Resolving the surface roughness and the TKE production process is usually very expensive so that wall models are often used in LES. In this work we did not intend to reproduce the exact process of the TKE production, because that is closely related to the detailed roughness geometry. Instead of that, this work is motivated by the recent research that the turbulent structures in the smooth-wall flows are determined by the mean shear (e.g., Tuerke and Jimenez [10] and Lozano-Duran and Bae [11]). Then we performed the simulations to examine whether the effect of roughness on the wall turbulence can be reproduced by imposing the rough-wall-like mean shear via CLES.

As the rough-wall-like mean shear is imposed uniformly in current CLES test cases, the mechanism of the TKE production is the same to the smooth wall case and the TKE equation remains unchanged, i.e., the TKE production is contributed only by the mean shear. Specifically, the TKE equation in CLES is

$$\begin{aligned}
 0 = & -\langle \tilde{u}'_i \tilde{u}'_j \rangle \frac{\partial \tilde{U}_i}{\partial x_j} - \tilde{U}_j \frac{\partial}{\partial x_j} \left\langle \frac{1}{2} \tilde{u}'_i \tilde{u}'_i \right\rangle - \frac{\partial}{\partial x_j} \left\langle \frac{1}{2} \tilde{u}'_i \tilde{u}'_i \tilde{u}'_j \right\rangle - \left\langle \frac{\partial \tilde{u}'_i \tilde{p}'}{\partial x_i} \right\rangle \\
 & + \frac{1}{Re} \frac{\partial^2}{\partial x_j \partial x_j} \left\langle \frac{1}{2} \tilde{u}'_i \tilde{u}'_i \right\rangle - \frac{1}{Re} \left\langle \frac{\partial \tilde{u}'_i}{\partial x_j} \frac{\partial \tilde{u}'_i}{\partial x_j} \right\rangle - \left\langle \tilde{u}'_i \frac{\partial \tau_{ij}}{\partial x_j} \right\rangle. \quad (16)
 \end{aligned}$$

The terms on the right-hand-side are the (resolved) production, the mean transport, the turbulent transport, the pressure dilation, the viscous diffusion, the (resolved) dissipation, and the SGS term. The tilde represents the values resolved in LES, the prime represents the fluctuation value, and the brackets represent the ensemble average.  $\tau_{ij}$  is the SGS stress. Comparing this equation to the smooth-wall TKE equation, the only difference comes from the SGS term. The SGS term can be further decomposed as follows:

$$-\left\langle \tilde{u}'_i \frac{\partial \tau_{ij}}{\partial x_j} \right\rangle = -\frac{\partial}{\partial x_j} \langle \tilde{u}'_i \tau_{ij} \rangle - \langle \tau_{ij} \rangle \frac{\partial \tilde{U}_i}{\partial x_j} + \langle \tau_{ij} \tilde{S}_{ij} \rangle. \quad (17)$$

The three terms on the right-hand side are the turbulent transport, the SGS production, and the SGS flux, respectively. Since the sum of the resolved Reynolds stress and the mean SGS stress is equal to the total Reynolds stress, the total production is

$$-\langle \tilde{u}'_i \tilde{u}'_j \rangle \frac{\partial \tilde{U}_i}{\partial x_j} - \langle \tau_{ij} \rangle \frac{\partial \tilde{U}_i}{\partial x_j} = -\langle u'_i u'_j \rangle \frac{\partial U_i}{\partial x_j} \quad (18)$$

In the present CLES,  $\langle \tau_{ij} \rangle$  is constrained uniformly to achieve the rough-wall-like mean shear so that the TKE production is affected via the modified mean shear  $\partial U_i / \partial x_j$ . Since the mean velocity profile is downward shifted in rough-wall flows, the mean shear  $\partial U_i / \partial x_j$  is reduced so that the TKE production is suppressed.

For the random and irregular roughness, Yuan and Piomelli [58] found that the spatial inhomogeneity of velocity and Reynolds stress results in the wake production, which will promote the wall-normal turbulent fluctuations. According to their DNS results, when the roughness height increases, the streamwise velocity fluctuation intensity is reduced while the peak values of the streamwise and the spanwise velocity fluctuation intensities remain unchanged. This is consistent with the present CLES results with the rough-wall-like mean shear although the wake production is not included. It indicates the wake production is relatively weak comparing to the mean shear production.

It also should be noted that the TKE production process is highly dependent on the detailed roughness geometry. Ikeda and Durbin [61] demonstrated that the coherent vortical structures can be formed just above the idealized roughness and result in strong TKE production. This indicates that prescribing the rough-wall-like mean shear is not enough to model the effect of the idealized roughness.

## VI. CONCLUSION

In this work, we have performed large-eddy simulations to examine the response of the wall turbulence when the rough-wall-like mean shear is imposed in the near-wall region of the channel flow. These numerical tests are carried out in the framework of CLES. Once the rough-wall-like mean shear is constrained, it is found that the downward shift of the mean velocity appears in the logarithmic and outer layer and the peak streamwise fluctuation intensity is reduced. Using the quadrant decomposition, the normalized Q4 (sweep) contribution to the Reynolds stress increases in the near-wall region. The two-point correlation of the streamwise velocity fluctuation is enhanced in the outer layer. These results demonstrate that the effect of imposing the rough-wall-like mean shear is similar to the effect of real surface roughness observed in previous research. Simulations with the equilibrium-wall model are also performed for comparison, and the results are qualitatively consistent with the present tests with the constrained mean shear. This indicates the approach of constraining the rough-wall-like mean shear can be used as a new wall model for the simulation of the rough-wall flow.

## ACKNOWLEDGMENTS

This work has been supported by NSFC (Grants No. 91752201 and No. 11988102), Shenzhen Science & Technology Program (Grant No. KQTD20180411143441009), Department of Science and Technology of Guangdong Province (Grants No. 2019B21203001, No. 2020B1212030001), Key Special Project for Introduced Talents Team of Southern Marine Science and Engineering Guangdong Laboratory (Guangzhou) (Grant No. GML2019ZD0103), and Outstanding Youth Science Foundation (Grant No. 11822208). Numerical simulations have been supported by Center for Computational Science and Engineering of Southern University of Science and Technology.

## APPENDIX A: FILTERING SCHEMES AND EDDY-VISCOSITY MODELS

Here we present the comparison of four different dynamic eddy-viscosity models [56,62,70,71] at  $Re_\tau = 590$ :

- (1) Plane-averaged dynamic Smagorinsky model (PADS).
- (2) Lagrangian-averaged dynamic Smagorinsky model (LADS).
- (3) Scale-dependent plane-averaged dynamic Smagorinsky model (SDPADS).
- (4) Scale-dependent Lagrangian-averaged dynamic Smagorinsky model (SDLADS).

We found that the discrete filter used in the dynamic models has a significant impact on the simulation results, thus the performance of five different discrete filters [72,73] are also compared:

TABLE I. Parameters and setup of the test cases for discrete filters based on the SDLADS model.

$Re_\tau$	$N_x \times N_y \times N_z$	Filter	$\tau_{ij}^m$	$k_s^+$
590	$64 \times 65 \times 64$	Tophat	SDLADS	0
590	$64 \times 65 \times 64$	Box(2)	SDLADS	0
590	$64 \times 65 \times 64$	Box(4)	SDLADS	0
590	$64 \times 65 \times 64$	Gaussian(2)	SDLADS	0
590	$64 \times 65 \times 64$	Gaussian(4)	SDLADS	0
590	$64 \times 65 \times 64$	Box(4)	PADS	0
590	$64 \times 65 \times 64$	Box(4)	LADS	0
590	$64 \times 65 \times 64$	Box(4)	SDPADS	0

- (1) Tophat filter.
- (2) Second-order box filter.
- (3) Fourth-order box filter.
- (4) Second-order Gaussian filter.
- (5) Fourth-order Gaussian filter.

First the eddy-viscosity model is fixed to SDLADS and then the discrete filter is fixed to the fourth-order box filter. The parameters and setup of the test cases are listed in Table I. Note that no constraint is imposed in these cases.

The mean velocity profile obtained with five discrete filters are shown in Fig. 12(a). The fourth-order box filter gives the best result in which the logarithmic region is accurately captured. Obvious log-layer mismatch is observed in the mean velocity profile obtained from the second-order box filter and the second-order Gaussian filter, and certain deviations also exist for the results obtained from the tophat filter and the fourth-order Gaussian filter. Thus the fourth-order box filter is selected as the only discrete filter for all other test cases.

As shown in Fig. 12(b), the log-layer mismatch occurs for the PADS, LADS, and SDPADS models. The mean velocity is overpredicted by the PADS and SDPADS models, while underpredicted by the LADS model. This is consistent with the numerical tests of Bou-Zeid *et al.* [56]. They found that the PADS and SDPADS models are underdissipative while the LADS model is overdissipative.

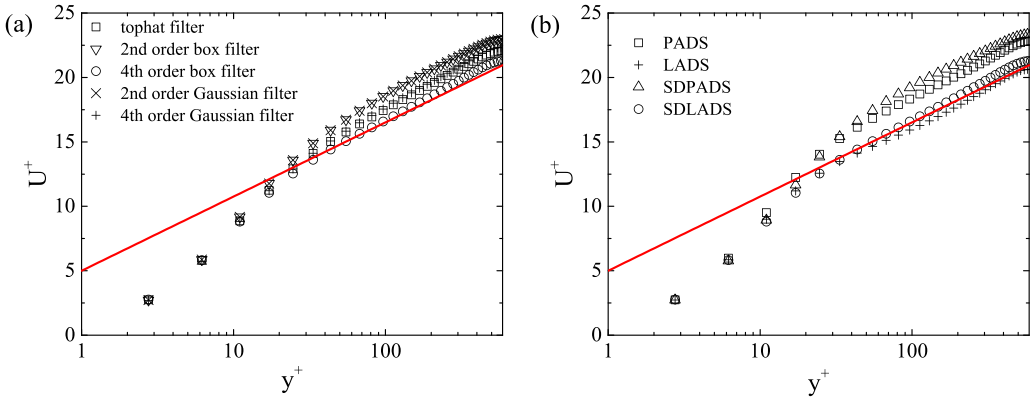


FIG. 12. Mean stream-wise velocity profile of the smooth wall channel flow at  $Re_\tau = 590$  simulated without constraint using (a) SDLADS model with five different discrete filters, (b) four different eddy-viscosity models with 4th order box filter. The solid line represents the log-law distribution  $U^+ = \kappa^{-1} \ln(y^+) + B$  for smooth wall flows.

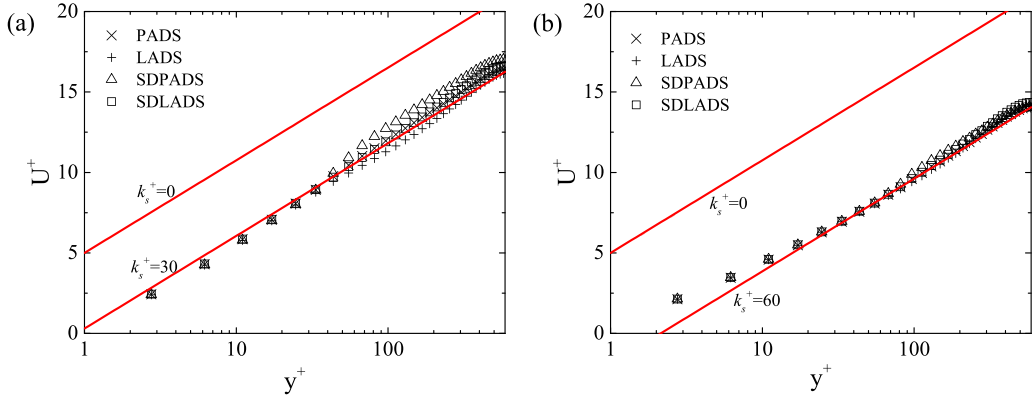


FIG. 13. Mean streamwise velocity profile of the channel flows with the constraint at  $Re_\tau = 590$ , (a)  $k_s^+ = 30$ , and (b)  $k_s^+ = 60$  with four basic SGS models. The dashed and solid lines are the logarithmic law for smooth and rough wall, respectively.

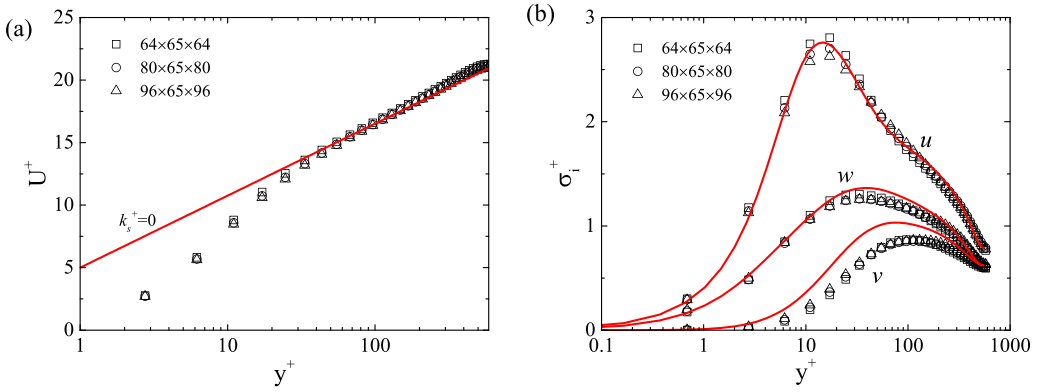


FIG. 14. (a) Mean streamwise velocity profile and (b) fluctuation intensities for  $k_s^+ = 0$ ,  $Re_\tau = 590$  obtained from various grid resolutions. The solid lines in (b) are DNS results [57].

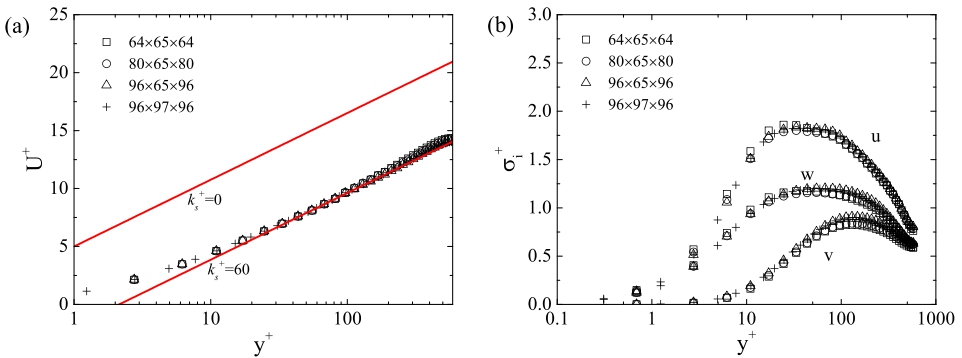


FIG. 15. (a) Mean streamwise velocity profile and (b) fluctuation intensities for  $k_s^+ = 60$ ,  $Re_\tau = 590$  obtained from various grid resolutions.

TABLE II. Parameters and setup of the test cases for various eddy-viscosity models under the constraint of mean stress.

$Re_\tau$	$N_x \times N_y \times N_z$	Filter	$\tau_{ij}^m$	$k_s^+$
590	$64 \times 65 \times 64$	Box(4)	PADS	30
590	$64 \times 65 \times 64$	Box(4)	LADS	30
590	$64 \times 65 \times 64$	Box(4)	SDPADS	30
590	$64 \times 65 \times 64$	Box(4)	SDLADS	30
590	$64 \times 65 \times 64$	Box(4)	PADS	60
590	$64 \times 65 \times 64$	Box(4)	LADS	60
590	$64 \times 65 \times 64$	Box(4)	SDPADS	60
590	$64 \times 65 \times 64$	Box(4)	SDLADS	60

The performance of these eddy-viscosity models under mean-stress constraint of  $k_s^+ = 30$  and  $k_s^+ = 60$  is tested, and the parameters and setup are shown in Table II. The downward shift of the mean velocity is observed for all the cases as shown in Figs. 13(a) and 13(b). Comparing to the smooth-wall test cases, the difference in the velocity profiles obtained by different eddy-viscosity models becomes smaller in the  $k_s^+ = 30$  cases and much more negligible in the  $k_s^+ = 60$  cases. This is reasonable since the near-wall constrained region is extended when  $k_s^+$  increases. As the mean velocity results from the integration of the mean stress, the model difference will be mitigated as the mean stress in a larger region is constrained.

## APPENDIX B: GRID DEPENDENCE CHECK

In previous discussions, we use the same grid resolution ( $N_x \times N_y \times N_z = 64 \times 65 \times 64$ ) for all the cases. This resolution is enough for  $Re_\tau = 180$  and  $Re_\tau = 590$  according to the fluctuation intensity and the spectrum of the streamwise velocity. Since most of our discussion is focused on  $Re_\tau = 590$ , we present further checks on the grid resolution to ensure the reliability of the simulation results. As shown in Table III, both the smooth- and rough-wall flows are simulated and constraint is imposed in the rough-wall simulation.

The mean velocity profiles and the fluctuation intensities are shown in Fig. 14 for the smooth-wall cases and in Fig. 15 for the rough-wall cases. Generally, the results almost remain unchanged when a finer grid is used. As shown in Fig. 14, the simulation results are all very close to the DNS results. Other statistics do not change much either when using more grid points in the simulation. For instance, the normalized quadrant contribution to the resolved Reynolds stress is shown in Fig. 16 for the grid resolutions of  $80 \times 65 \times 80$  and  $96 \times 65 \times 96$ . The increased contributions of the Q4 events are observed just like that in Fig. 6. Changes might be observed but the essential difference between the smooth- and rough-wall flows has already been captured by the grid  $64 \times 65 \times 64$ ,

TABLE III. The parameters and setup of the simulations for the grid dependence check.

$Re_\tau$	$k_s^+$	$N_x \times N_y \times N_z$	$\tau_{ij}^m$
590	0	$64 \times 65 \times 64$	SDLADS
590	0	$80 \times 65 \times 80$	SDLADS
590	0	$96 \times 65 \times 96$	SDLADS
590	60	$64 \times 65 \times 64$	SDLADS
590	60	$80 \times 65 \times 80$	SDLADS
590	60	$96 \times 65 \times 96$	SDLADS
590	60	$96 \times 97 \times 96$	SDLADS

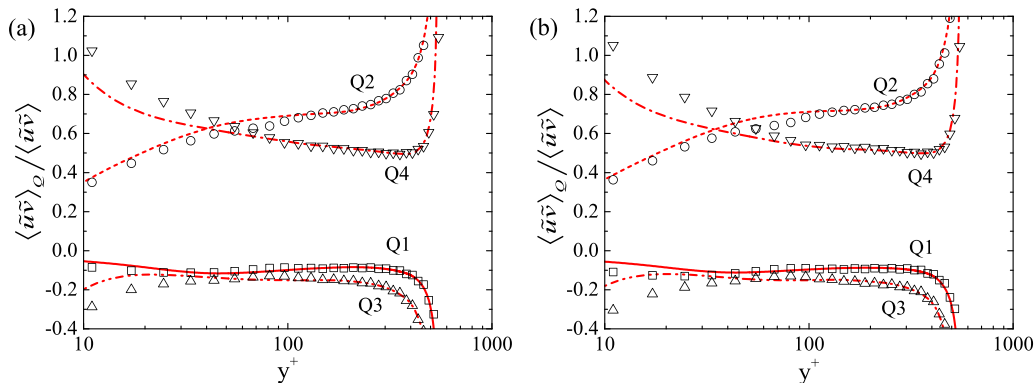


FIG. 16. Comparison of the normalized quadrant contribution to the resolved Reynolds stress in smooth ( $k_s^+ = 0$ , lines) and rough-wall ( $k_s^+ = 60$ , symbols) flows with the grid ( $N_x \times N_y \times N_z$ ) (a)  $80 \times 65 \times 80$ , (b)  $96 \times 65 \times 96$ .

which is enough for the present LES at  $Re_\tau = 590$  when the proper eddy-viscosity model and proper discrete filter are used.

- 
- [1] J. Nikuradse, Laws of flow in rough pipes, NACA Technical Memorandum, Report No. NACA-TM-1292, 1933.
  - [2] C. F. Colebrook, Turbulent flow in pipes, with particular reference to the transitional region between smooth and rough wall laws, *J. Inst. Civ. Eng.* **11**, 133 (1939).
  - [3] L. F. Moody, Friction factors for pipe flow, *Trans. ASME* **66**, 671 (1944).
  - [4] M. P. Schultz, The relationship between frictional resistance and roughness for surfaces smoothed by sanding, *J. Fluids Eng.* **124**, 492 (2002).
  - [5] M. R. Raupach and A. S. Thom, Turbulence in and above plant canopies, *Annu. Rev. Fluid Mech.* **13**, 97 (1981).
  - [6] J. Finnigan, Turbulence in plant canopies, *Annu. Rev. Fluid Mech.* **32**, 519 (2000).
  - [7] R. E. Britter and S. R. Hanna, Flow and dispersion in urban areas, *Annu. Rev. Fluid Mech.* **35**, 469 (2003).
  - [8] H. J. S. Fernando, Fluid dynamics of urban atmospheres in complex terrain, *Annu. Rev. Fluid Mech.* **42**, 365 (2010).
  - [9] J. Jimenez, Coherent structures in wall-bounded turbulence, *J. Fluid Mech.* **842**, P1 (2018).
  - [10] F. Tuerke and J. Jimenez, Simulations of turbulent channels with prescribed velocity profiles, *J. Fluid Mech.* **723**, 587 (2013).
  - [11] A. Lozano-Duran and H. J. Bae, Characteristic scales of Townsend's wall-attached eddies, *J. Fluid Mech.* **868**, 698 (2019).
  - [12] P. Davidson and P.-A. Krogstad, A universal scaling for low-order structure functions in the log-law region of smooth- and rough-wall boundary layers, *J. Fluid Mech.* **752**, 140 (2014).
  - [13] H. J. Bae, A. Lozano-Duran, S. T. Bose, and P. Moin, Dynamic slip wall model for large-eddy simulation, *J. Fluid Mech.* **859**, 400 (2019).
  - [14] S. Chen, Z. Xia, S. Pei, J. Wang, Y. Yang, Z. Xiao, and Y. Shi, Reynolds-stress-constrained large-eddy simulation of wall-bounded turbulent flows, *J. Fluid Mech.* **703**, 1 (2012).
  - [15] J. Jimenez and P. Moin, The minimal flow unit in near-wall turbulence, *J. Fluid Mech.* **225**, 213 (1991).
  - [16] J. Jimenez, Turbulent flows over rough walls, *Annu. Rev. Fluid Mech.* **36**, 173 (2004).
  - [17] M. R. Raupach, Conditional statistics of Reynolds stress in rough-wall and smooth-wall turbulent boundary layers, *J. Fluid Mech.* **108**, 363 (1981).



- [18] P.-A. Krogstad, R. A. Antonia, and L. W. B. Browne, Comparison between rough- and smooth-wall turbulent boundary layers, *J. Fluid Mech.* **245**, 599 (1992).
- [19] P.-A. Krogstad and R. A. Antonia, Surface roughness effects in turbulent boundary layers, *Exp. Fluids* **27**, 450 (1999).
- [20] M. P. Schultz and K. A. Flack, The rough-wall turbulent boundary layer from the hydraulically smooth to the fully rough regime, *J. Fluid Mech.* **580**, 381 (2007).
- [21] S.-H. Lee and H. J. Sung, Direct numerical simulation of the turbulent boundary layer over a rod-roughened wall, *J. Fluid Mech.* **584**, 125 (2007).
- [22] P.-A. Krogstad and V. Efron, About turbulence statistics in the outer part of a boundary layer developing over two-dimensional surface roughness, *Phys. Fluids* **24**, 075112 (2012).
- [23] P.-A. Krogstad and R. A. Antonia, Structure of turbulent boundary layers on smooth and rough walls, *J. Fluid Mech.* **277**, 1 (1994).
- [24] R. J. Volino, M. P. Schultz, and K. A. Flack, Turbulence structure in rough- and smooth-wall boundary layers, *J. Fluid Mech.* **592**, 263 (2007).
- [25] M. R. Raupach, R. A. Antonia, and S. Rajagopalan, Rough-wall turbulent boundary layers, *Appl. Mech. Rev.* **44**, 1 (1991).
- [26] A. A. Townsend, *The Structure of Turbulent Shear Flow*, 2nd ed. (Cambridge University Press, Cambridge, UK, 1976).
- [27] M. F. Tachie, D. J. Bergstrom, and R. Balachandar, Rough wall turbulent boundary layers in shallow open channel flow, *J. Fluids Eng.* **122**, 533 (2000).
- [28] S. Leonardi, P. Orlandi, R. J. Smalley, L. Djenidi, and R. A. Antonia, Direct numerical simulations of turbulent channel flow with transverse square bars on one wall, *J. Fluid Mech.* **491**, 229 (2003).
- [29] K. Bhaganagar, J. Kim, and G. Coleman, Effect of roughness on wall-bounded turbulence, *Flow, Turbul. Combust.* **72**, 463 (2004).
- [30] A. E. Perry and M. S. Chong, On the mechanism of wall turbulence, *J. Fluid Mech.* **119**, 173 (1982).
- [31] K. A. Flack, M. P. Schultz, and T. A. Shapiro, Experimental support for Townsend's Reynolds number similarity hypothesis on rough walls, *Phys. Fluids* **17**, 035102 (2005).
- [32] G. J. Kunkel and I. Marusic, Study of the near-wall-turbulent region of the high-Reynolds-number boundary layer using an atmospheric flow, *J. Fluid Mech.* **548**, 375 (2006).
- [33] I. P. Castro, Rough-wall boundary layers: Mean flow universality, *J. Fluid Mech.* **585**, 469 (2007).
- [34] L. Chan, M. MacDonald, D. Chung, N. Hutchins, and A. Ooi, A systematic investigation of roughness height and wavelength in turbulent pipe flow in the transitionally rough regime, *J. Fluid Mech.* **771**, 743 (2015).
- [35] D. T. Squire, C. Morrill-Winter, N. Hutchins, M. P. Schultz, J. C. Klewicki, and I. Marusic, Comparison of turbulent boundary layers over smooth and rough surfaces up to high Reynolds numbers, *J. Fluid Mech.* **795**, 210 (2016).
- [36] R. J. Volino, M. P. Schultz, and K. A. Flack, Turbulence structure in a boundary layer with two-dimensional roughness, *J. Fluid Mech.* **635**, 75 (2009).
- [37] R. J. Volino, M. P. Schultz, and K. A. Flack, Turbulence structure in boundary layers over periodic two- and three-dimensional roughness, *J. Fluid Mech.* **676**, 172 (2011).
- [38] K. A. Flack and M. P. Schultz, Roughness effects on wall-bounded turbulent flows, *Phys. Fluids* **26**, 101305 (2014).
- [39] R. H. Kraichnan, Decimated amplitude equations in turbulence dynamics, in *Theoretical Approaches to Turbulence*, edited by D. L. Dwoyer, M. Y. Hussaini, and R. G. Voigt (Springer, New York, 1985), pp. 91–135.
- [40] R. H. Kraichnan and S. Chen, Is there a statistical mechanics of turbulence? *Physica D* **37**, 160 (1989).
- [41] Z.-S. She and E. Jackson, Constrained Euler System for Navier-Stokes Turbulence, *Phys. Rev. Lett.* **70**, 1255 (1993).
- [42] Y. Shi, Z. Xiao, and S. Chen, Constrained subgrid-scale stress model for large eddy simulation, *Phys. Fluids* **20**, 011701 (2008).
- [43] L. Biferale, F. Bonaccorso, M. Buzicotti, and K. P. Iyer, Self-Similar Subgrid-Scale Models for Inertial Range Turbulence and Accurate Measurements of Intermittency, *Phys. Rev. Lett.* **123**, 014503 (2019).

- [44] Z. Xia, Y. Shi, R. Hong, Z. Xiao, and S. Chen, Constrained large-eddy simulation of separated flow in a channel with streamwise-periodic constrictions, *J. Turb.* **14**, 1 (2013).
- [45] Z. Jiang, Z. Xiao, Y. Shi, and S. Chen, Constrained large-eddy simulation of wall-bounded compressible turbulent flows, *Phys. Fluids* **25**, 106102 (2013).
- [46] R. Hong, Z. Xia, Y. Shi, Z. Xiao, and S. Chen, Constrained large-eddy simulation of compressible flow past a circular cylinder, *Commun. Comput. Phys.* **15**, 388 (2014).
- [47] Z. Xia, Z. Xiao, Y. Shi, and S. Chen, Mach number effect of compressible flow around a circular cylinder, *AIAA J.* **54**, 2004 (2016).
- [48] Y. Zhao, Z. Xia, Y. Shi, Z. Xiao, and S. Chen, Constrained large-eddy simulation of laminar-turbulent transition in channel flow, *Phys. Fluids* **26**, 095 (2014).
- [49] S. Chen, Y. Chen, Z. Xia, K. Qu, Y. Shi, Z. Xiao, Q. Liu, Q. Cai, U. Li, C. Lee, R. Zhang, and J. Cai, Constrained large-eddy simulation and detached eddy simulation of flow past a commercial aircraft at 14 degrees angle of attack, *Sci. China: Phys. Mech. Astron.* **56**, 270 (2013).
- [50] J. C. Rotta, Turbulent boundary layers in incompressible flow, *Prog. Aero. Sci.* **2**, 1 (1962).
- [51] T. Cebeci and K. C. Chang, Calculation of incompressible rough-wall boundary-layer flows, *AIAA J.* **16**, 730 (1978).
- [52] S. Patil and D. Tafti, Two-layer wall model for large-eddy simulations of flow over rough surfaces, *AIAA J.* **50**, 454 (2012).
- [53] P.-A. Krogstad, Modification of the van Driest damping function to include the effects of surface roughness, *AIAA J.* **29**, 888 (1991).
- [54] U. Piomelli and E. Balaras, Wall-layer models for large-eddy simulations, *Annu. Rev. Fluid Mech.* **34**, 349 (2002).
- [55] X. I. A. Yang, J. Sadique, R. Mittal, and C. Meneveau, Integral wall model for large eddy simulations of wall-bounded turbulent flows, *Phys. Fluids* **27**, 025112 (2015).
- [56] E. Bou-Zeid, C. Meneveau, and M. Parlange, A scale-dependent Lagrangian dynamic model for large eddy simulation of complex turbulent flows, *Phys. Fluids* **17**, 025105 (2005).
- [57] J. Jimenez and S. Hoyas, Turbulent fluctuations above the buffer layer of wall-bounded flows, *J. Fluid Mech.* **611**, 215 (2008).
- [58] J. Yuan and U. Piomelli, Roughness effects on the Reynolds stress budgets in near-wall turbulence, *J. Fluid Mech.* **760**, R1 (2014).
- [59] P. S. Jackson, On the displacement height in the logarithmic velocity profile, *J. Fluid Mech.* **111**, 15 (1981).
- [60] K. Bhaganagar and L. Chau, Characterizing turbulent flow over 3-D idealized and irregular rough surfaces at low Reynolds number, *Appl. Math. Model.* **39**, 6751 (2015).
- [61] T. Ikeda and P. Durbin, Direct simulations of a rough-wall channel flow, *J. Fluid Mech.* **571**, 235 (2007).
- [62] F. Porte-Agel, C. Meneveau, and M. B. Parlange, A scale-dependent dynamic model for large-eddy simulation: Application to a neutral atmospheric boundary layer, *J. Fluid Mech.* **415**, 261 (2000).
- [63] J. M. Wallace, Quadrant analysis in turbulence research: History and evolution, *Annu. Rev. Fluid Mech.* **48**, 131 (2016).
- [64] S. S. Lu and W. W. Willmarth, Measurements of the structure of the Reynolds stress in a turbulent boundary layer, *J. Fluid Mech.* **60**, 481 (1973).
- [65] M. Heisel, T. Dasari, Y. Liu, J. Hong, F. Coletti, and M. Guala, The spatial structure of the logarithmic region in very-high-Reynolds-number rough wall turbulent boundary layers, *J. Fluid Mech.* **857**, 704 (2018).
- [66] R. J. Adrian, C. D. Meinhart, and C. D. Tomkins, Vortex organization in the outer region of the turbulent boundary layer, *J. Fluid Mech.* **422**, 1 (2000).
- [67] K. Fukagata, K. Iwamoto, and N. Kasagi, Contribution of Reynolds stress distribution to the skin friction in wall-bounded flows, *Phys. Fluids* **14**, L73 (2002).
- [68] R. B. Dean, Reynolds number dependence of skin friction and other bulk flow variables in two-dimensional rectangular duct flow, *J. Fluids Eng.* **100**, 215 (1978).
- [69] C. Cheng, W. Li, A. Lozano-Duran, and H. Liu, Identity of attached eddies in turbulent channel flows with bidimensional empirical mode decomposition, *J. Fluid Mech.* **870**, 1037 (2019).

- [70] D. K. Lilly, A proposed modification of the Germano subgrid-scale closure method, [Phys. Fluids](#) **4**, 633 (1992).
- [71] C. Meneveau, T. S. Lund, and W. H. Cabot, A Lagrangian dynamic subgrid-scale model of turbulence, [J. Fluid Mech.](#) **319**, 353 (1996).
- [72] P. Sagaut and R. Grohens, Discrete filters for large eddy simulation, [Int. J. Numer. Meth. Fluids](#) **31**, 1195 (1999).
- [73] M. Pino Martin, U. Piomelli, and G. V. Candler, Subgrid-scale models for compressible large-eddy simulations, [Theor. Comput. Fluid Dyn.](#) **13**, 361 (2000).